J. Fluid Mech. (2008), *vol.* 617, *pp.* 255–281.
doi:10.1017/S0022112008004187 Printed in the United Kingdom

Lagrangian measurements of inertial particle accelerations in a turbulent boundary layer

S. GERASHCHENKO, N. S. SHARP, S. NEUSCAMMAN AND Z. WARHAFT†

Sibley School of Mechanical and Aerospace Engineering, Cornell University, Ithaca, NY 14853, USA
and International Collaboration for Turbulence Research

(Received 23 May 2008 and in revised form 4 September 2008)

Two-dimensional Lagrangian acceleration statistics of inertial particles in a turbulent boundary layer with free-stream turbulence are determined by means of a particle tracking technique using a high-speed camera moving along the side of the wind tunnel at the mean flow speed. The boundary layer is formed above a flat plate placed horizontally in the tunnel, and water droplets are fed into the flow using two different methods: sprays placed downstream from an active grid, and tubes fed into the boundary layer from humidifiers. For the flow conditions studied, the sprays produce Stokes numbers varying from 0.47 to 1.2, and the humidifiers produce Stokes numbers varying from 0.035 to 0.25, where the low and high values refer to the outer boundary layer edge and the near-wall region, respectively. The Froude number is approximately 1.0 for the sprays and 0.25 for the humidifiers, with a small variation within the boundary layer. The free-stream turbulence is varied by operating the grid in the active mode as well as a passive mode (the latter behaves as a conventional grid). The boundary layer momentum-thickness Reynolds numbers are 840 and 725 for the active and passive grid respectively. At the outer edge of the boundary layer, where the shear is weak, the acceleration probability density functions are similar to those previously observed in isotropic turbulence for inertial particles. As the boundary layer plate is approached, the tails of the probability density functions narrow, become negatively skewed, and their peak occurs at negative accelerations (decelerations in the streamwise direction). The mean deceleration and its root mean square (r.m.s.) increase to large values close to the plate. These effects are more pronounced at higher Stokes number. In the vertical direction, there is a slight downward mean deceleration and its r.m.s., which is lower in magnitude than that of the streamwise component, peaks in the buffer region. Although there are free-stream turbulence effects, and the complex boundary layer structure plays an important role, a simple model suggests that the acceleration behaviour is dominated by shear, gravity and inertia. The results are contrasted with inertial particles in isotropic turbulence and with fluid particle acceleration statistics in a boundary layer. The background velocity field is documented by means of hot-wire anemometry and laser Doppler velocimetry measurements. These appear to be the first Lagrangian acceleration measurements of inertial particles in a shear flow.

1. Introduction

The objective of this paper is to study the Lagrangian acceleration statistics of small (sub-Kolmogorov scale) particles with densities much greater than that of the

---

† Email address for correspondence: zw16@cornell.edu

surrounding fluid (inertial particles) in a turbulent boundary layer. While significant attention has been given to the study of Lagrangian acceleration statistics in flows without shear (Toschi & Bodenschatz 2009), flows with more complex forcing have received comparatively little attention.

Understanding the Lagrangian behaviour of inertial particles in inhomogeneous flows has important practical and conceptual implications. The formation of raindrops in clouds occurs in a highly inhomogeneous turbulent medium. The inertial effects cause clustering of small droplets and this may enhance the droplet growth rate (Shaw 2003; Lehmann *et al.* 2007; Ghosh *et al.* 2005). The clustering is affected by both the magnitude and relative time scale (to that of the turbulence) of the inertial particle accelerations, and thus in order to understand clustering mechanisms, it is necessary to study inertial particle acceleration statistics (Toschi & Bodenschatz 2009; Bec *et al.* 2006; Ayyalasomayajula, Collins & Warhaft 2008). In the oceans zooplankton predators perceive their prey from a Lagrangian perspective and the way in which the phytoplankton move and distribute themselves is in part determined by the turbulence (Seuront & Schmitt 2004). In engines the combustion of the fuel droplets is affected by particle inertia (Post & Abraham 2002) as are particle deposition, entrainment and re-suspension rates in a turbulent boundary layer (Marchioli & Soldati 2002). All of these flows are inhomogeneous at the large scale and shear is often an important driving mechanism. In many situations the particle size is small. For example in clouds coalescing droplets are order of 10 μm while the Kolmogorov scale is of order 1 mm. From a fundamental viewpoint it is known that large-scale inhomogeneity affects the turbulence structure down to the very smallest (Kolmogorov) scales (Shen & Warhaft 2000; Ouellette *et al.* 2006*b*) and thus it is important to study Lagrangian acceleration and related statistics in these more complex flows under controlled laboratory conditions.

Recently there have been significant advances in the measurement, computation and theory of fluid particle trajectories (small particles of the same density as the surrounding fluid) in turbulence. These have been largely due to experimental developments in high-speed tracking devices such as optical imaging (Bourgoin *et al.* 2006; Salazar *et al.* 2008), silicon strip detectors (Voth *et al.* 2002) and acoustic techniques (Mordant *et al.* 2001) in conjunction with the development of turbulence generating devices that can obtain the high Reynolds numbers needed for the exploration of theoretical postulates (Makita 1991; Mydlarski & Warhaft 1996; Mordant *et al.* 2001; Voth *et al.* 2002).

These Lagrangian measurements have provided insight into particle accelerations and their statistics, including the acceleration probability density function (p.d.f.) (Voth *et al.* 2002), Lagrangian structure functions (Xu *et al.* 2006) and particle pair dispersion (Bourgoin *et al.* 2006) in flows that are close to isotropic. By tracking particles, the full acceleration, its temporal plus spatial variation, can be determined. The more traditional Eulerian measurements, while providing important information on the velocity field $U_i(t)$, cannot easily yield the full acceleration $a_i(t) = \partial U_i/\partial t + U_j \partial U_i/\partial x_j$. There have been some indirect attempts to determine acceleration using the Eulerian approach. Using fourth-order structure functions Hill & Wilczak (1995), Gylfason, Ayyalasomayajula & Warhaft (2004) and Gulitski *et al.* (2007) have deduced the acceleration variance in isotropic turbulence from hot-wire anemometry (HWA) measurements. Lehmann, Nobach & Tropea (2002) and Kinzel *et al.* (2006) have used laser Doppler velocimetry (LDV) techniques to measure acceleration by estimating the change in signal frequency in time and Lowe & Simpson (2006) using an advanced LDV technique, have deduced the correlation between the velocity and acceleration, an important quantity in the Reynolds transport equations. Recently an extended laser Doppler technique has been used to study weakly inertial particles and bubble accelerations in Kármán flow (Volk *et al.* 2008). Other measurements of Lagrangian and Eulerian accelerations have been performed using particle image velocimetry (PIV) (Jakobsen, Dewhirst & Greated 1997; Jensen *et al.* 2001; Christensen & Adrian 2002; Dong *et al.* 2001; Liu & Katz 2006); however these techniques are limited to small spatial volumes and residence times. Finally, Tsuji *et al.* (2007) have measured the pressure fluctuations and from the gradient of this quantity the acceleration may be calculated if viscous effects are unimportant. Despite these advances, directly following a fluid particle has many advantages over PIV and LDV measurements if information on acceleration and related statistics is required over significant spatial volumes and times. The Lagrangian approach also allows the study of multi-particle statistics, which is vital for our understanding of dispersion and the statistical geometry of turbulent flows (Xu, Ouellette & Bodenschatz 2008), and for the study of inertial particles, the subject addressed here.

Inertial particles react in a more complex way than do fluid particles to variations in the surrounding fluid motion. Recent direct numerical simulations (DNS) (Bec *et al.* 2006), measurements (Ayyalasomayajula *et al.* 2006) and modelling (Ayyalasomayajula *et al.* 2008) of inertial particles significantly smaller than the Kolmogorov scale in isotropic turbulence, show that the inertial effects reduce the particle acceleration variance and attenuate the tails of the acceleration p.d.f. (By contrast, for inertial particles with sizes greater than the Kolmogorov scale, athough the variance is reduced, the tails of the p.d.f. are less affected (Xu & Bodenschatz 2008; Volk *et al.* 2008.) A similar observation has been made for neutrally buoyant large particles (Qureshi *et al.* 2007).) For the sub-Kolmogorov inertial particles the observation of reduced variance and attenuated p.d.f. tails is consistent with the particles preferentially concentrating away from regions of intense vortex motion into regions of high strain due to the centrifugal forces acting on them (Maxey & Riley 1983; Maxey 1987; Squires & Eaton 1991; Sundaram & Collins 1997). For recent experimental evidence of clustering see Wood, Hwang & Eaton (2005); Saw *et al.* (2008); Salazar *et al.* (2008). While the observations are clear, the physics has been interpreted in various ways. These include the clustering of acceleration stagnation points (Chen, Goto & Vassilicos 2006), a sweep–stick mechanism (Goto & Vassilicos 2008), instability in the particle spatial distribution (Elperin *et al.* 2002) and filtering of low-inertia particles (Ayyalasomayajula *et al.* 2008). Thus although the clustering of sub-Kolmogorov inertial particles is well established there is still considerable discussion on the precise mechanisms. Understanding the particle acceleration statistics is an important step in this direction.

So far there has been no attempt to look at inertial particles in shear using high-speed Lagrangian tracking techniques, although there has been a significant body of work on other aspects of particles in shear such as particle deposition, trapping and segregation in boundary layers (e.g. Freidlander & Johnstone 1957; Brooke *et al.* 1992; Kaftori, Hetsroni & Banerjee 1995*a*, *b*; Marchioli & Soldati 2002; Kulick, Fessler & Eaton 1994). Here we address the following question: *How does the presence of shear affect the Lagrangian acceleration statistics of inertial particle motion?* Our objective is to compare the results obtained in shear flow with those observed in isotropic turbulence. As noted, there is significant practical as well as fundamental interest in this problem.

In order to address this question we track the motion of water droplets in a wind tunnel in which a flat plate is placed to provide a turbulent boundary layer and thus a high degree of shear close to the wall. As in Ayyalasomayoula *et al.* (2006), we inject the particles into the flow from sprays downstream from an active grid. We also use an additional injection technique for particles with low inertia, by injecting the particles directly into the boundary layer downstream of the leading edge, and we show that there is consistency with the results of the spray system. Both methods provide a homogeneous distribution of water droplets in the boundary layer. In these experiments there are high levels of free-stream turbulence above the boundary layer. These are significant flows in their own right but perhaps not as generic as the boundary layer in a laminar free-stream flow. Thus we carefully document the flow by means of HWA and LDV measurements. We will be reporting the details of these interesting flows in another publication. Here we show that as we alter the free-stream turbulence level we do not find a qualitative change in the particle characteristics near the plate. Thus although our flow is not simple, we see it as a first step in the study of the effects of shear on particles with inertia.

The effects of inertia are described by the Stokes number, $St=\tau_s/\tau_\eta$, the ratio of the particle inertial response time (stopping time) $\tau_s=(1/18)(\rho_d/\rho_f)d^2/\nu$ to the time scale of the smallest eddies (Kolmogorov time) $\tau_\eta=(\nu/\epsilon)^{1/2}$, where ρ_d, ρ_f, d, ν and ϵ are the particle density (1000 kg m^{-3}), fluid density (1.2 kg m^{-3}), particle diameter, fluid kinematic viscosity (1.5×10^{-5} m^2 s^{-1}) and turbulence dissipation rate respectively. Thus $St\sim d^2\epsilon^{1/2}$ for a fixed density ratio and fluid viscosity, and for particles with low Reynolds number (as is the case for the present work). Inertial effects are most pronounced for St of order one (Wood *et al.* 2005; Aliseda *et al.* 2002) but they may be important even for values as low as 0.01 (Chun *et al.* 2005). By minimizing the particle size, the inertia can be reduced to small values, so that the droplets behave as fluid particles.

Gravity also affects the motion of inertial particles (Aliseda *et al.* 2002). The measure of its effect in turbulence is the ratio of the Stokes terminal velocity $u_g=\tau_s g$ to the Komogorov velocity $u_\eta=\eta/\tau_\eta$, where g and η are the acceleration due to gravity and Kolmogorov length scale $(\nu^3/\epsilon)^{1/4}$ respectively. The sole governing parameter for the turbulence itself is the Reynolds number. Here we use the Taylor-scale Reynolds number, $Re_\lambda=\langle u^2\rangle^{1/2}\lambda/\nu$, to describe the free-stream conditions and the momentum-thickness Reynolds number, $Re_\theta=U_0\theta/\nu$, for the boundary layer. Here $\langle u^2\rangle^{1/2}$ is the longitudinal fluctuating velocity r.m.s., λ is the Taylor microscale $([U^2\langle u^2\rangle/\langle(\partial u/\partial t)^2\rangle]^{1/2})$, U_0 is the free-stream velocity and θ is the momentum thickness.

The outline of the paper is as follows. First we describe the experimental set-up and diagnostics. In § 3 we characterize the flow, its mean and variance velocity characteristics by means of HWA measurements. We compare and contrast these results to the zero free-stream turbulence boundary layer measurements of DeGraaff & Eaton (2000). In § 4 we present the results of our acceleration measurements in the lower part of the boundary layer where shear is dominant. We describe the mean and variance acceleration profiles and the acceleration p.d.f. distributions as a function of height above the plate and contrast these to the case of isotropic turbulence. Finally in § 5 we provide a simple model based on the equation of motion for an inertial particle to explain our results.

2. Apparatus

The experiments were conducted in a 1 m × 0.9 m × 20 m open-circuit wind tunnel with an active grid consisting of randomly flipping triangular agitator wings attached to rotating grid bars (Mydlarski & Warhaft 1996) placed at the entrance to the tunnel

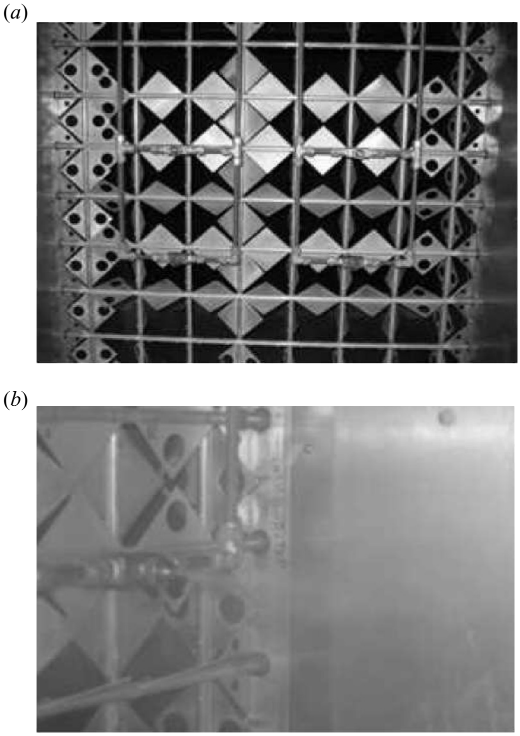

FIGURE 1. The apparatus used to produce the large particles ($\langle d^2\rangle_0^{1/2} = 41\,\mu\text{m}$, $St_0 = 0.47$) with sprays placed 5 cm downstream of the active grid. (*a*) The spray system downstream from the active grid; (*b*) close up of the particles generated from the spray nozzles.

test section (figure 1). The grid creates large-scale, high-intensity turbulence. In order to produce a boundary layer at the height level of the camera diagnostics, a flat glass plate of size 3.3 m × 0.67 m × 0.012 m was placed 0.4 m above the floor of the tunnel, 0.9 m from the grid. The measurements of the particles were taken 2.7 m from the leading edge of the plate (i.e. 3.6 m from the grid) and 0.5 m from the tunnel sidewall. Due to the fixed tunnel cross-section area there was a small favourable pressure gradient in the x-direction.

Two methods of producing water droplets were used. To produce high Stokes number droplets, an array of four nozzles (Ayyalasomayajula *et al.* 2006; Gylfason 2006) was symmetrically placed 5 cm downstream from the grid (figure 1) although only the two lower sprays were used for the present experiment with the boundary layer plate in place. The spray system consists of small (1 mm diameter) nozzles fed on one side by water and the other by compressed air to cause spray breakup and mixing (Spraying System Co. Illinois. Series 1/4 J). The velocity of the air and water at the nozzle exit was $8\,\text{m}\,\text{s}^{-1}$ and $13\,\text{m}\,\text{s}^{-1}$ respectively. The droplets produced by this method had a maximum free-stream Stokes number $St_0 = 0.47$, where the subscript zero refers to the stream conditions. The sprays had an effect on the velocity field due to the excess momentum introduced at the nozzles by the air–water jet combination but we were unable to observe any abnormal behaviour of the flow at the measurement station, which is about 100 Kolmogorov time scales (and 200 stopping times, τ_s) from the jet. This is ample time for mixing by the active grid. Figure 2 shows the longitudinal velocity spectrum measured with and without the

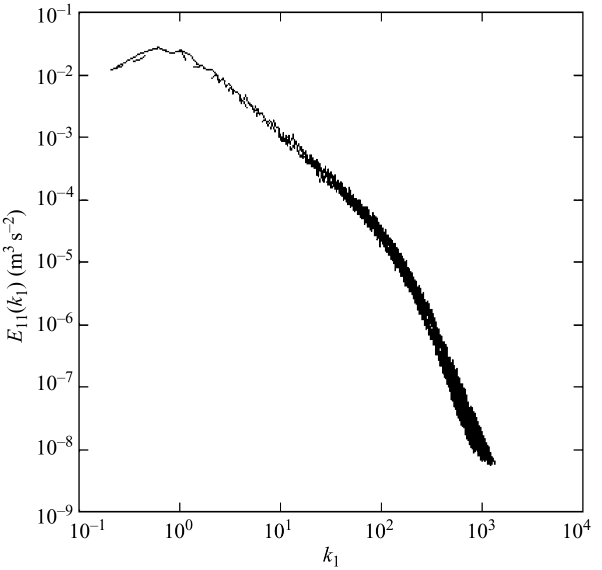

FIGURE 2. The longitudinal velocity spectrum measured with the air jets from the sprays on (solid line) and off (dashed line) at the location of the particle tracking measurements. $Re_{\lambda 0} = 240$ (see table 2 below for flow parameters).

air sprays operating. There is no effect on the quality of the spectrum, indicating that the air jet had evened out at the measuring station, but the mean increased slightly (by around 3–4 %). When the air/water sprays were operating together, at the measurement station the LDV measured an increase of nearly 10 % in the mean over the case for the spray system not operating. This we attribute to the further added momentum from the water sprays as well as to some bias in the LDV which selectively samples the faster particles in high-intensity turbulence (Fuchs, Nobach & Tropea 1994). We note that experiments with smaller (fluid) particles using a similar spray system (Ayylasomayajula *et al.* 2008, figure 1) were able to reproduce the particle acceleration p.d.f.s consistent with those of Voth *et al.* (2002) and Bec *et al.* (2006), providing further indication that the initial conditions were not influencing the acceleration results at the measurement location. For further discussion on the effect of the sprays on clustering see Saw *et al.* (2008).

In order to feed low Stokes number droplets into the boundary layer we used ultrasonic commercial humidifiers (Sunbeam Products Inc.). Tubes (diameter 3 cm) connected to these humidifiers were fed to the middle of the plate, 7.5 cm above the plate and 1.6 m from the measurement location (figure 3). The droplets produced by this method had low Stokes numbers ($St_0 = 0.07$ and $St_0 = 0.035$ for two different Reynolds numbers studied). It will be shown that the Stokes number varies in the boundary because of its dependence on the turbulence dissipation rate. The tubes had some effect on the boundary layer characteristics (§ 3). In all experiments the particle mass loading was low (approximately 10^{-4} kg water per kg of dry air).

A high-speed camera (Phantom v7.1) attached to a precision, linearly translating, pneumatically driven sled (Gylfason 2006) was accelerated to the mean flow speed and moved at a constant speed, with less than 0.5 % variation over the measurement length (measured by means of an optical encoder, Gylfason 2006). The camera frame rate was 8000 frames per second with a resolution of 512 pixels × 512 pixels. A fibre

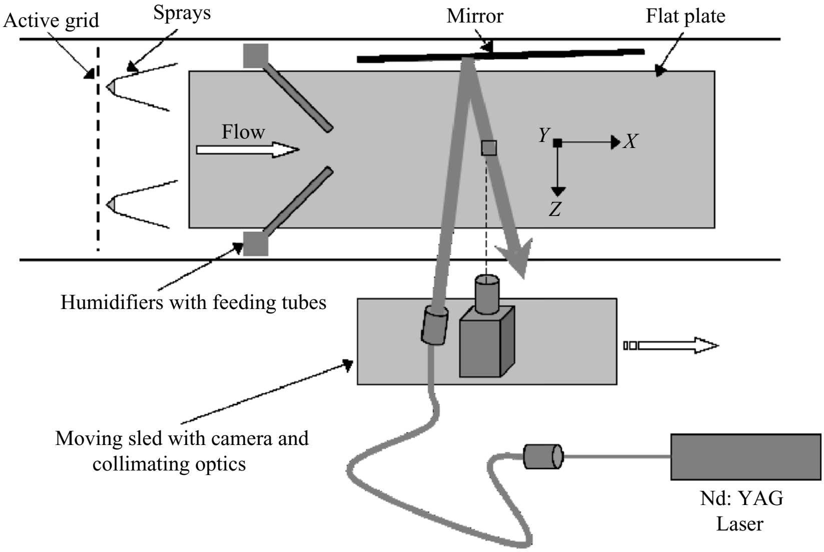

FIGURE 3. Schematic of the forward scatter experiment (top view). The two separate methods of introducing the droplets are shown together. When the sprays are operating, the humidifiers and feeding tubes are removed from the tunnel. The y coordinate is measured vertically from the plate.

optic cable was attached to the moving camera and a laser beam (Nd-YAG laser, 20 W, pulse width 120 ns at a repetition rate of 40 KHz) was reflected from a mirror at the far side of the tunnel so that forward scatter was effected at an angle of about 5° (figure 3). The aperture of the camera objective was completely open to achieve a small depth of focus ($\approx$2 mm). Only the particles in focus were analysed. Out of focus particles were discarded based on intensity thresholding. The background obtained by averaging many images was subtracted from all images before analysis. The laser beam forward scatter arrangement provided a stronger scattered signal from the particles than the laser sheet arrangement used in Ayyalasomayajula *et al.* (2006). This was the reason why it was chosen in the current experiments. In § 4 we compare the results using the two different methods.

The camera tracked the particles over a distance of 50 cm. The sampling area was 3.3 cm × 3.3 cm. The inter-sample time was 0.0125 and 0.0042 Kolmogorov time units for the high and low Reynolds number cases respectively ($Re_{\lambda 0} = 240$ and 100, see table 2 below) and the corresponding spatial resolution was 0.148 and 0.097 Komogorov lengths. The total number of sled runs varied from 1500 to 3000 resulting in 5×10^5 to 10^6 tracks or approximately 40×10^6 to 90×10^6 acceleration estimates. A given track length was order 2 to $5\tau_{\eta 0}$ and assuming that the accelerations are correlated over a full Kolmogorov time scale, we estimate the total number of independent accelerations to be of order 5×10^5 to 2×10^6. The field of view was divided into strips (see the following paragraph) resulting in independent samples ranging from 3×10^4 for the smallest strips to 4×10^5 for the largest strips for the case $St_0 = 0.47$, $Re_{\lambda 0} = 240$ and slightly smaller for the lower St and Re cases. The p.d.f. results described below suggest that this is a rather conservative estimate since they are well resolved to approximately 10^{-5}. The data were analysed following the particle tracking algorithm developed by the Bodenschatz group (Voth *et al.* 2002; Ouellette, Xu & Bodenschatz 2006*a*). Although over a particular run the camera

y^+	6	7.5	18	37	62	87	129	186	244
Δy^+	0–12	0–15	12–25	25–50	50–75	75–100	100–158	158–215	215–273

TABLE 1. Strip widths at different distances from the plate.

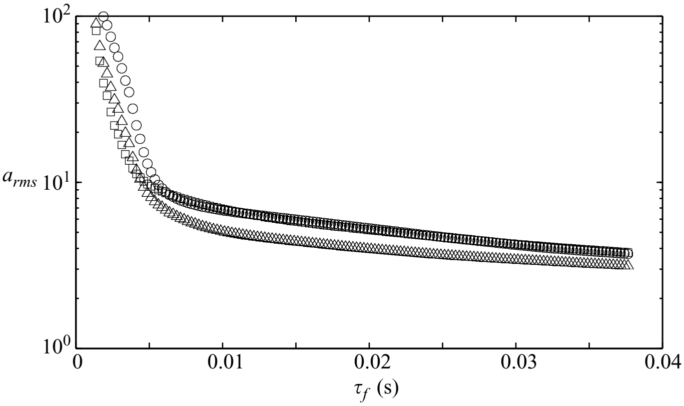

FIGURE 4. The dependence of a_{rms} on fit time τ_f at $y^+ = 244$. □, $Re_{\lambda 0} = 240$, $St_0 = 0.47$; ○, $Re_{\lambda 0} = 240$, $St_0 = 0.07$; △, $Re_{\lambda 0} = 100$, $St_0 = 0.035$.

speed was steady, from run to run there was a small variation in its mean motion. Thus we did not extract longitudinal velocity statistics from the particle tracks. The relative camera motion does not affect acceleration because it is a second derivative. Velocity statistics from static probes are reported in § 3.

The accelerations were calculated by convolution of the measured particle tracks with a Gaussian smoothing and differentiating filter (Mordant, Crawford & Bodenschatz 2004). Then the area of the 3.3 cm × 3.3 cm boundary layer image was divided into strips of varying thickness and the accelerations were binned according to their locations in order to study their statistics at various levels in the boundary layer. The widths of the strips in y^+ units are shown in table 1. Their widths were varied to see if the acceleration variance and other statistics were affected, but we will show that, if the variation of strip width was reasonable (in the sense that it did not average too large a part of the boundary layer), the statistics were not affected.

In the measurements of Voth *et al.* (2002), the best fit interval, τ_f (the time of a particle trajectory over which the acceleration is determined) to use to obtain the acceleration, was of order the Kolmogorov time (Voth *et al.* 2002, p. 143). For larger τ_f the fit does not correspond to the real trajectory and underestimates the acceleration, and for smaller τ_f the fit mostly corresponds to the position measurement errors and overestimates the acceleration. Voth *et al.* (2002) showed that the acceleration r.m.s. is best obtained by extrapolation of the fit interval to zero provided the particle trajectories are long enough (about $10\tau_\eta$ or more). Figure 4 shows the dependence of the acceleration r.m.s. on the fit interval, τ_f, for the widest strip ($\Delta y^+ = 215$–273) for different Re and St. The a_{rms} dependence corresponds well with the Voth *et al.* (2002, figure 23) measurements. However, in order to determine the acceleration r.m.s. at smaller heights in the boundary layer, because of smaller strip width we were unable to employ the Voth *et al.* (2002) method of extrapolating the τ_f to zero.

$Re_{\lambda 0}$	U_0 ($\mathrm{m\,s^{-1}}$)	$(\langle u^2\rangle^{1/2}/\langle U\rangle)_0$	ϵ_0 ($\mathrm{m^2\,s^{-3}}$)	η_0 (mm)	$\tau_{\eta 0}$ (s)	u^* ($\mathrm{m\,s^{-1}}$)	δ (cm)	δ_ν (mm)	Re_θ	Re^*
100	2.37	4.7 %	0.0176	0.66	0.03	0.117	6.09	0.128	725	470
240	2.39	11.6 %	0.098	0.43	0.01	0.124	9.97	0.12	840	830

TABLE 2. Free-stream and boundary layer parameters (zero subscripts refer to the free stream). u^* is the friction velocity; δ is the thickness of the boundary layer based on 99.5 % of the free-stream velocity; $\delta_\nu = \nu/u^*$ is the viscous length scale; $Re^* = u^*\delta/\nu$ is wall stress Reynolds number; $\epsilon = 15(\nu/U^2)\langle(\partial u/\partial t)^2\rangle$ is the turbulence energy dissipation rate.

Instead, we chose the value of τ_f just before the interval where the noise became significant. This occurs at $\tau_f \approx 0.01$ s (figure 4). We used this value in our calculations of the accelerations and their statistics presented in § 4. It corresponds to $\tau_f \approx \tau_{\eta 0}$ for $Re_{\lambda 0} = 240$ and $\tau_f \approx 0.3\tau_{\eta 0}$ for $Re_{\lambda 0} = 100$. From our estimates and from the analysis done by Voth *et al.* (2002) it follows that the acceleration r.m.s. calculated for the finite time is smaller by approximately 5–15 % (depending on *St*) than the real r.m.s. when τ_f goes to zero. There is also a resolution error in the determination of the particle position. In the particle tracking algorithm employed here the position of a particle is determined from the peak in the Gaussian fit of a particle intensity profile. This, in general, can give a sub-pixel resolution of the particle position. But in practice the intensity profile is not always Gaussian, and this particularly affects the resolution of the larger particles, limiting them to a resolution of about 1 pixel. This gives an uncertainty in the tracks, and results in an uncertainty in the acceleration for our smaller particles, $\langle d^2\rangle^{1/2} = 16\,\mu\mathrm{m}$, to be about $1\,\mathrm{m\,s^{-2}}$. For the $\langle d^2\rangle^{1/2} = 41\,\mu\mathrm{m}$ particles this uncertainty is larger, about $2.4\,\mathrm{m\,s^{-2}}$. (See § 4 for the particle distributions.) Both the larger particle size and the over-saturated particle intensity profile reduce the accuracy of the Gaussian fit. We estimated that the resolution error is larger than the error introduced by determining the acceleration over a finite time. The error bars will be shown in § 4.

The longitudinal and vertical velocity components were measured with an X-array HWA (TSE 1241) with 3.05 μm tungsten wires. Supplementary measurements of the streamwise and vertical velocity were made with an LDV system (TSI Incorporated).

3. Flow characterization: the velocity field

The flow is a flat-plate boundary layer with free-steam turbulence. The particle injection mechanisms have been described in § 2. Here we characterize the flow using both HWA and LDV.

We define the flows in terms of their free-stream turbulence Taylor-scale Reynolds numbers, $Re_{\lambda 0}$. There are two cases. In the first case with the active grid operating, for the free-stream turbulence $Re_{\lambda 0} = 240$. In the second case with the active grid turned off, such that the grid structure acted like a passive grid (with the winglets placed in the same direction as the flow and thus providing no extra flow impedance), $Re_{\lambda 0} = 100$. The boundary layer Reynolds numbers based on the wall stress and momentum thickness at the measurement location, as well as other relevant flow parameters are listed in table 2. The particles injected from the humidifiers ($St_0 = 0.07$ and 0.035 for $Re_{\lambda 0} = 240$ and 100 respectively) had negligible effect on the velocity statistics although the tubes from which the particles were fed disturbed the velocity field. This is discussed below. The spray system ($St_0 = 0.47$, $Re_{\lambda 0} = 240$) did affect the

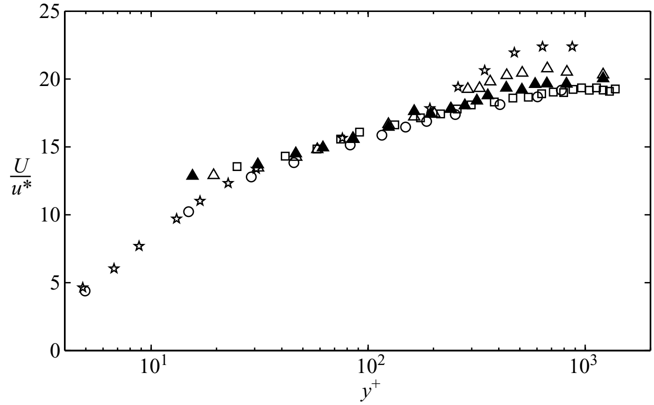

FIGURE 5. Mean velocity profiles in the streamwise direction, normalized by the friction velocity: ▲, $Re_{\lambda 0} = 100$, $Re_\theta = 660$ (measured with HWA, without humidifier tubes in place); △, $Re_{\lambda 0} = 100$, $Re_\theta = 725$ (HWA, with humidifier tubes in place); □, $Re_{\lambda 0} = 240$, $Re_\theta = 840$ (HWA, without humidifier tubes in place); ○, $Re_{\lambda 0} = 240$, $Re_\theta = 840$ (LDV, with humidifier tubes in place); ☆ $Re_{\lambda 0} = 0$, $Re_\theta = 1430$ (DeGraaff & Eaton 2000).

velocity field (see §2). The velocity field profiles (figures 5, 6 and 7) are for the sprays turned off.

Figure 5 shows the mean velocity profiles normalized by wall units: $U^+ \equiv U/u^*$, $y^+ \equiv yu^*/\nu$. We are primarily concerned with the region of significant mean shear in the turbulence regime, i.e. from approximately $y^+ = 10$ to $y^+ = 250$. For reference we have compared with the zero free-stream turbulence boundary layer data of DeGraaff & Eaton (2000). Because of the free-stream turbulence, the outer velocity defect region is diminished ($Re_{\lambda 0} = 100$) or disappears entirely ($Re_{\lambda 0} = 240$). This is consistent with data of Hancock & Bradshaw (1989) and Thole & Bogard (1996). Our data for the logarithmic region are consistent with DeGraaff & Eaton (2000). We believe the small departure at $y^+ \approx 20$ is due to the interference of the plate with the HWA probe. The LDV resolves the flow better close to the wall and is consistent with the DeGraaff & Eaton (2000) measurements. Notice that we have included the mean flow profiles for the flow with and without the humidifiers tubes in place. There is no apparent effect on the mean profiles. We will show that the tubes do have some effect on the fluctuations.

The variance profiles of the u (streamwise) and v (vertical) components and the uv covariance profiles are shown in figure 6. The $Re_{\lambda 0} = 100$ case follows the zero free-stream-turbulence data well for the u (longitudinal) variance (figure 6*a*). For the v (vertical) variance there is a departure, but the magnitudes of the $Re_{\lambda 0} = 100$ case and the zero free-stream-turbulence case are similar, particularly close to the wall. Of course far from the plate the present measurements approach their free-stream turbulence levels while the De Graaff & Eaton measurements approach zero. The $Re_{\lambda 0} = 240$ case departs significantly from the zero free-stream turbulence data above $y^+ \approx 20$ for the u component and above $y^+ \approx 100$ for the v component. The covariance profiles for both $Re_{\lambda 0} = 100$ and $Re_{\lambda 0} = 240$ (figure 6*b*) are qualitatively similar to the zero free-stream turbulence case although the magnitudes are lower and there is significant scatter in $Re_{\lambda 0} = 100$ case.

The tubes introducing the low Stokes number particles into the flow had no measurable effect on the high Reynolds number ($Re_{\lambda 0} = 240$) free-stream turbulence flow. For the low Reynolds number flow ($Re_{\lambda 0} = 100$), there was a measurable effect,

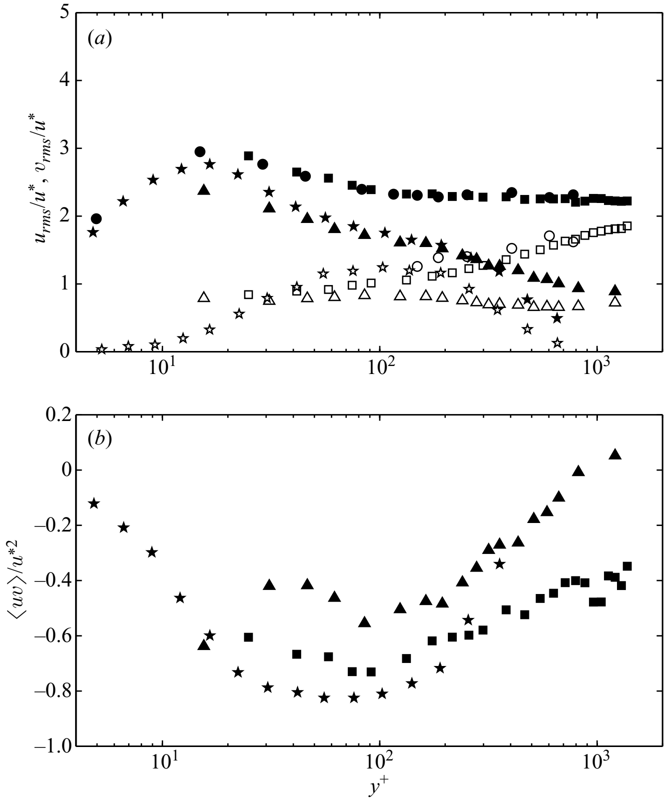

FIGURE 6. (*a*) u_{rms}/u^* (filled symbols) and v_{rms}/u^* (open symbols), (*b*) Reynolds stresses normalized by the friction velocity. For both graphs: triangles, $Re_{\lambda 0} = 100$, $Re_\theta = 660$ (HWA, without humidifier tubes in place); squares, $Re_{\lambda 0} = 240$, $Re_\theta = 840$ (HWA, without humidifier tubes in place); circles, $Re_{\lambda 0} = 240$, $Re_\theta = 840$ (LDV, with humidifier tubes in place); stars, $Re_{\lambda 0} = 0$, $Re_\theta = 1430$ (DeGraaff & Eaton 2000).

particularly in the outer part of the boundary layer although the results with and without the tubes in place are qualitatively similar (figure 7). The effect of the small particles from the humidifiers on the velocity field was negligible. This was checked by measuring with HWA (humidifiers turned off) and then with LDV (humidifiers turned on). As discussed in § 2 the larger Stokes number particles from the sprays did have an effect on the velocity field due to the excess momentum introduced at the nozzles by the air–water jet combination. We estimate that this increased the Stokes number by approximately 5 %.

In summary, the low free-stream turbulence boundary layer flow does not depart significantly from that of the zero free-stream turbulence boundary layer below $y^+ \approx 300$ from the plate (although there are some departures because of the presence of the tubes feeding in the particles) while for the high Reynolds number free-stream flow, the free-stream turbulence affects the flow down to $y^+ \approx 20$. We will show that the dominant mechanism affecting the inertial particles is the presence of the mean shear. We will shown in a future publication that the mean shear and dissipation are the dominant terms in the energy budget near the wall in the present flows, as they are for zero free-stream turbulence boundary layers.

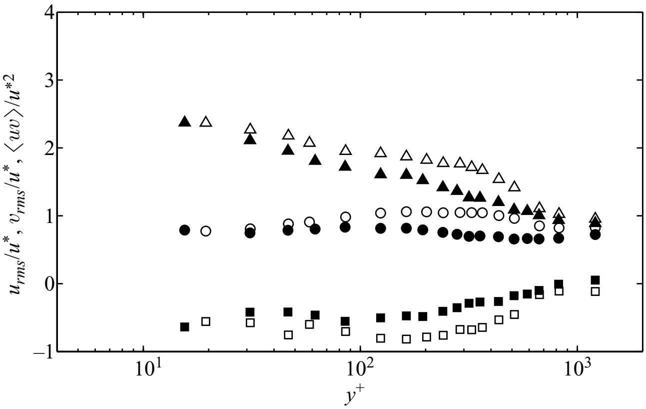

FIGURE 7. Comparison of the profiles for $Re_{\lambda 0} = 100$ with (open symbols) and without (filled symbols) humidifier tubes in place: triangles, u_{rms}/u^*; circles, v_{rms}/u^*; squares, $\langle uv\rangle/u^{*2}$.

4. The particle acceleration statistics

We varied the Stokes number for two different flow conditions. For the high free-stream turbulence produced by the active grid ($Re_{\lambda 0} = 240$), we used two different particle injection methods: first, the sprays placed close to the grid (figure 1) produced a high free-stream Stokes number ($St_0 = 0.47$); and, second, the tubes introduced low Stokes number particles ($St_0 = 0.07$) directly into the boundary layer (figure 3). The third flow condition is for the low free-stream turbulence case produced by the passive grid ($Re_{\lambda 0} = 100$). Here we introduced the low Stokes number particles ($St_0 = 0.035$) by the second injection method. Thus we can compare two different Stokes numbers at the same Reynolds number, and two different Reynolds numbers at approximately the same Stokes number. Note that although the humidifier system was at the same setting for both $Re_{\lambda 0} = 240$ and $Re_{\lambda 0} = 100$, because the dissipation rate was higher for the former case (figure 9*b* below), St_0 was also greater (0.07 for $Re_{\lambda 0} = 240$ compared with 0.035 for $Re_{\lambda 0} = 100$). We will sometimes refer to these as the 'low Stokes' number case, since although they are different by a factor two, they are an order of magnitude lower than the high Stokes number ($St_0 = 0.47$) case.

We begin by showing the particle size distributions for the two different particle injection methods, determined by a phase Doppler particle analyser located at the same position as the acceleration measurements (figure 8). The particles are poly-dispersed with a significantly broader distribution for the larger particles. We were careful to have enough illumination to capture the full distribution, particularly for the small particles. The profiles of the variation of the particle size and Stokes number as a function of y^+ for the three different conditions are shown in figure 9. The variation in size is weak (figure 9*a*), with a slight increase in size as the wall is approached which may be due to gravity-induced gradient effects. Because the turbulence dissipation rate increases as the wall is approached (figure 9*b*, inset) and $St \sim d^2\epsilon^{1/2}$, the Stokes number increases with decreasing y^+ (figure 9*b*). Thus the particles not only encounter increasing shear as the wall is approached, but their inertial effects increase as well. Further, the effects of gravity are also significant. In figure 10 we show the ratio u_g/u_η. It is of order one for the $St_0 = 0.47$ case but decreases as the wall is approached due to the increase in the turbulence dissipation rate ($u_g/u_\eta \sim d^2\epsilon^{-1/4}$). For the low Stokes number cases the slight growth in the particle diameter (figure 9*a*) offsets the growth in the dissipation rate (figure 9*b*), causing little variation in u_g/u_η.

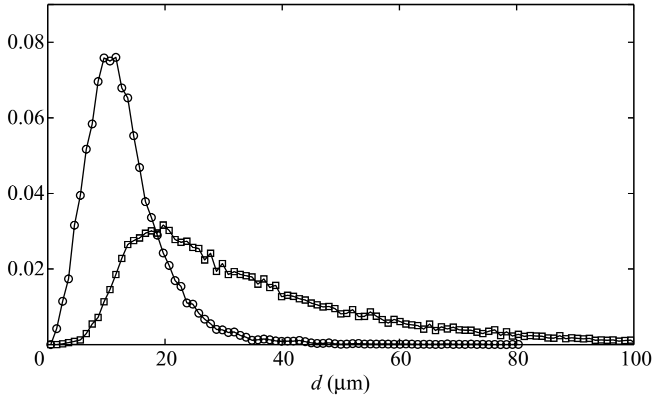

FIGURE 8. The distributions of particles sizes measured in the outer part of the boundary layer at $Re_{\lambda 0} = 240$. □, $\langle d^2 \rangle_0^{1/2} = 41\,\mu\mathrm{m}$, $St_0 = 0.47$; ○, $\langle d^2 \rangle_0^{1/2} = 16\,\mu\mathrm{m}$, $St_0 = 0.07$. As in Ayyalasomayajula *et al.* (2006) the particle size was determined from the second moment of the distribution. The values based on the first moment were 39.5 μm and 14.5 μm.

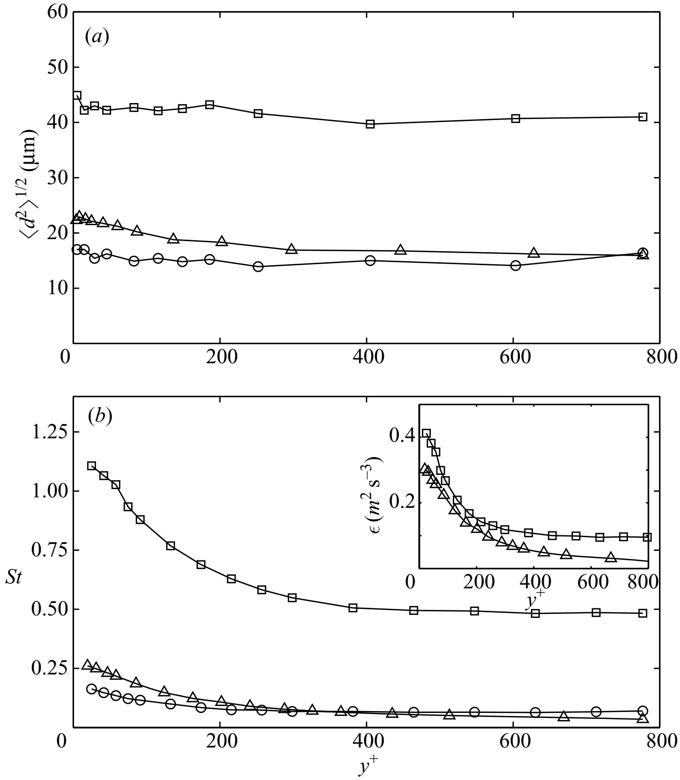

FIGURE 9. (*a*) Size distribution of particles as function of distance from the plate, (*b*) Stokes number dependence on distance from the plate: □, $\langle d^2 \rangle_0^{1/2} = 41\,\mu\mathrm{m}$, $Re_{\lambda 0} = 240$; ○, $\langle d^2 \rangle_0^{1/2} = 16\,\mu\mathrm{m}$, $Re_{\lambda 0} = 240$; △, $\langle d^2 \rangle_0^{1/2} = 16\,\mu\mathrm{m}$, $Re_{\lambda 0} = 100$. Inset in (*b*) dissipation rate dependance on distance from the plate from HWA measurements: □, $Re_{\lambda 0} = 240$; △, $Re_{\lambda 0} = 100$.

The p.d.f.s of the particles as a function of y^+ are shown in figure 11 for the three cases. Before discussing their variation within the boundary layer, we will compare their value at the outer edge, $y^+ = 244$, where the p.d.f.s are approaching their free-stream values (although there is still some residual skewness, figure 15) with existing

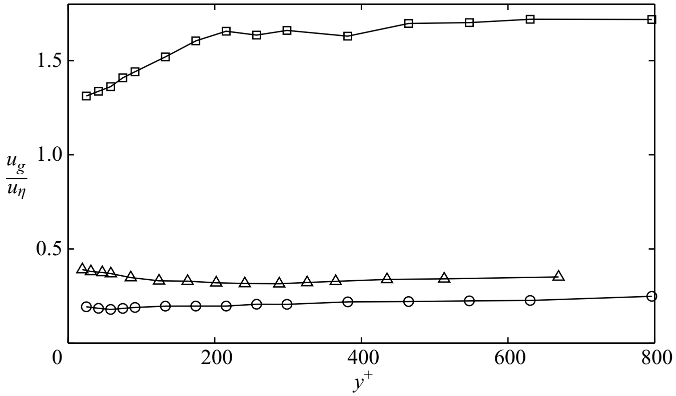

FIGURE 10. Ratio of the gravitational velocity to Kolmogorov velocity: □, $Re_{\lambda 0} = 240$, $St_0 = 0.47$; ○, $Re_{\lambda 0} = 240$, $St_0 = 0.07$; △, $Re_{\lambda 0} = 100$, $St_0 = 0.035$.

DNS and experimental results for isotropic turbulence. In figure 11(*a*) we compare our p.d.f.s with the isotropic DNS computations of Bec *et al.* (2006). We have plotted their case of $St = 0.48$, $Re_\lambda = 185$. This is closest in Stokes and Reynolds numbers to our $St_0 = 0.47$, $Re_{\lambda 0} = 240$ case. The DNS p.d.f.s are slightly wider than ours, but both are significantly narrower than for the $St = 0$ case (Bec *et al.* 2006; Ayyalasomayajula *et al.* 2008; Voth *et al.* 2002). Note that the DNS are for mono-dispersed particles and our particles are poly-dispersed and this, as well as the idealization used for particle behaviour in the DNS (the Bec *et al.* 2006 DNS only applies to the fluid phase; see Elgobashi & Truesdell 1992 for a discussion of the relative importance of the other terms in the equation of motion), may account for the difference. For the lower Stokes number (figure 11*b*), we have plotted the free-stream experimental results of Ayyalasomayajula *et al.* (2006) from the same wind tunnel; $St_0 = 0.09$, $Re_{\lambda 0} = 250$ in decaying (isotropic) turbulence. We note that the Ayyalasomayajula *et al.* (2006) experiment was carried out using a light sheet with 30° forward scatter. In the present work we are using nearly zero degrees forward scatter (figure 3). There is good agreement between the two methods. Thus we are satisfied that we have a baseline for which shear effects are minimal to compare with results where the shear becomes more pronounced as the wall is approached. For the lowest Stokes number case, $St_0 = 0.035$, $Re_{\lambda 0} = 100$ (figure 11*c*), the p.d.f.s are slightly narrower than for the other low Stokes number case (figure 11*b*). Here the lower Reynolds number may be playing a role (figure 12 below). We note that for the $St = 0.07$ case, the p.d.f. is narrower than for fluid particles at the same Reynolds number (Ayyalasomayajula *et al.* 2008, figure 1), and the variance is reduced by approximately 15 %, suggesting that inertial effects are still significant even at this low Stokes number.

With decreasing y^+, the x component of the acceleration p.d.f. becomes skewed, narrower, and its peak moves to the left, indicating a mean negative acceleration (figure 11). The narrowing of the p.d.f. appears to be a Stokes number effect. It is more pronounced for the $St_0 = 0.47$ case than for the two lower Stokes number cases. Whether the narrowing due to inertia is the sole cause is not clear; the shear may also play a role. The skewness of the p.d.f.s clearly indicates the preponderance of decelerating effects over positive acceleration. We will quantify this below. The acceleration p.d.f. of the y component also narrowed and became skewed, but there was little shift in the peak. We do not present the y component p.d.f.s here but show their skewness below.

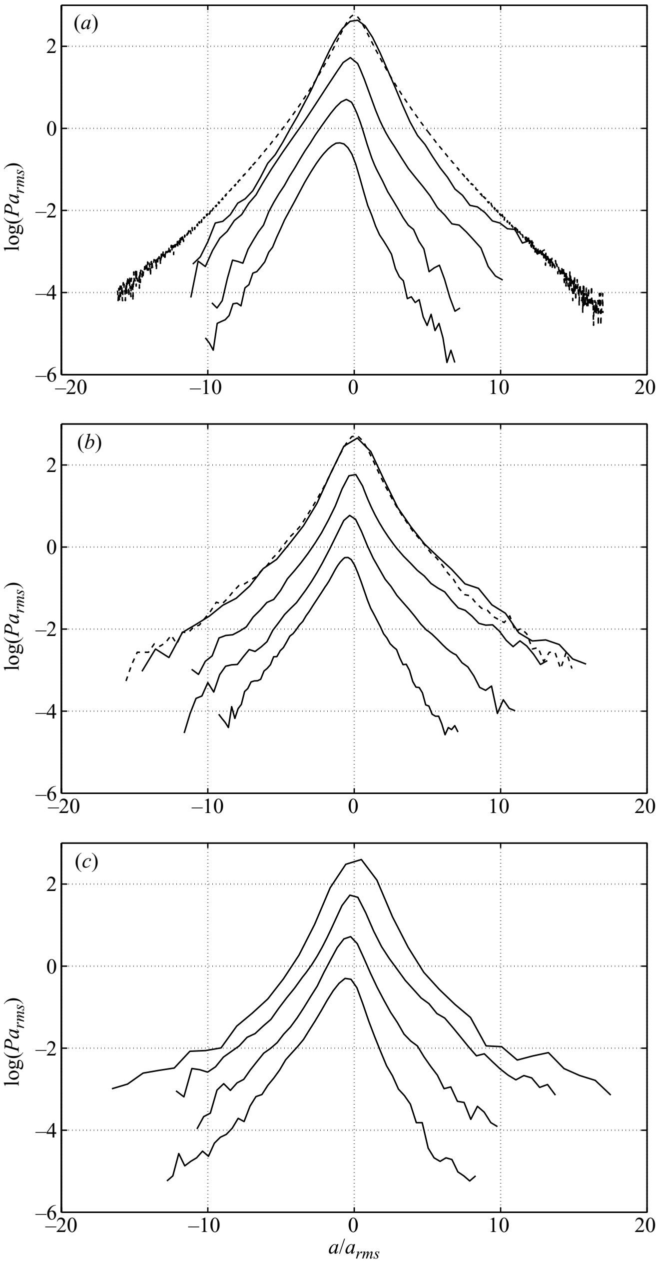

FIGURE 11. Normalized p.d.f.s of x component total acceleration (including the mean). (a) $St_0 = 0.47$, $Re_{\lambda 0} = 240$ (solid lines), $St_0 = 0.48$, $Re_{\lambda 0} = 185$ (Bec *et al.* 2006, dashed line); (b) $St_0 = 0.07$, $Re_{\lambda 0} = 240$ (solid lines); $St_0 = 0.09$, $Re_{\lambda 0} = 250$ (Ayyalasomayajula *et al.* 2006, dashed line); (c) $St_0 = 0.035$, $Re_{\lambda 0} = 100$. For all plots from top to bottom: $y^+ = 244; 37; 18; 7.5$. The plot at $y^+ = 7.5$ is not staggered and the rest are successively moved up by one unit.

Before describing the mean and r.m.s. acceleration profiles, we compare Stokes and Reynolds number effects. In figure 12 we show the acceleration p.d.f.s for our high and low Stokes number cases at the same Reynolds number, and for our high and low free-stream Reynolds number cases at approximately the same Stokes number. These

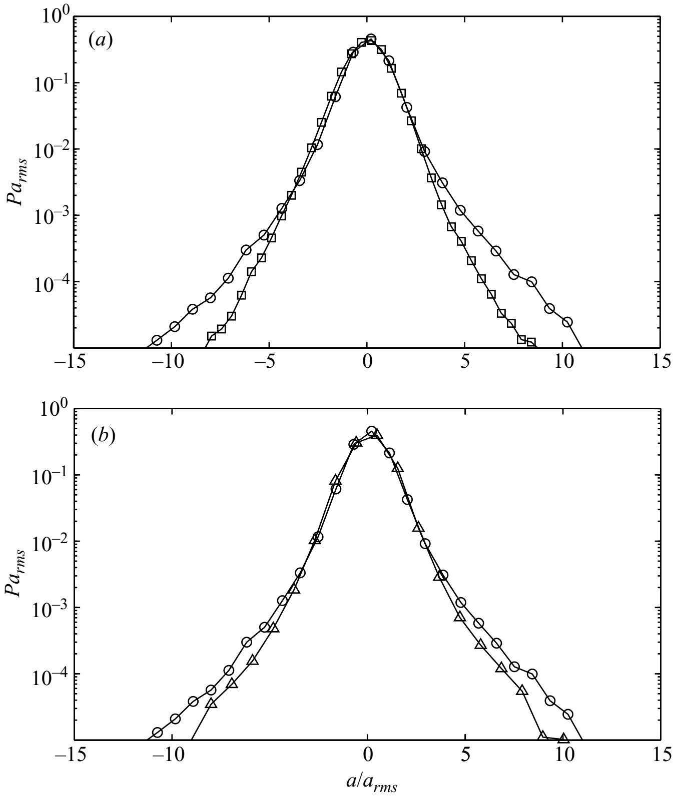

FIGURE 12. Normalized acceleration p.d.f.s of x components at $y^+ = 244$: (*a*) different Stokes numbers at the same Reynolds number, (*b*) different Reynolds numbers at the same Stokes number (see the Stokes number match at $y^+ = 244$, figure 9*b*). □, $St_0 = 0.47$, $Re_{\lambda 0} = 240$; ○, $St_0 = 0.07$, $Re_{\lambda 0} = 240$; △, $St_0 = 0.035$, $Re_{\lambda 0} = 100$.

are taken from figure 11 at $y^+ = 244$. At this height in the boundary layer the p.d.f.s are approximately symmetric because shear effects are small. There are clear Stokes and Reynolds number effects with the tails becoming narrower as either the Stokes number increases (figure 12*a*) or as the Reynolds number decreases (figure 12*b*). These results are consistent with previous observations and DNS (Ayyalasomayajula *et al.* 2006; Bec *et al.* 2006) in isotropic turbulence. The narrowing of the p.d.f. with Reynolds number is due to the lower turbulence intensity, and hence the decrease in rare, high-acceleration events (Bec *et al.* 2006; Voth *et al.* 2002). As discussed in § 1, the narrowing of the tails with increasing Stokes number is thought to be due to the inertial particles selectively sampling the fluid field: they are less likely to experience regions of the fluid undergoing the large accelerations that occur in regions of high vorticity.

The mean profiles of the x and y accelerations are shown in figures 13. The shift of the peaks of the p.d.f.s (figure 11) corresponds well with the mean accelerations shown in figure 13, although not exactly: in figure 13 we plot mean values of acceleration while the peaks in figure 11 are the most probable values. In the free stream the mean accelerations must be zero, and this is shown to be the case. As the wall is approached, the mean accelerations in the streamwise component become negative. The effect is most pronounced in the high Stokes number case. Clearly inertial effects

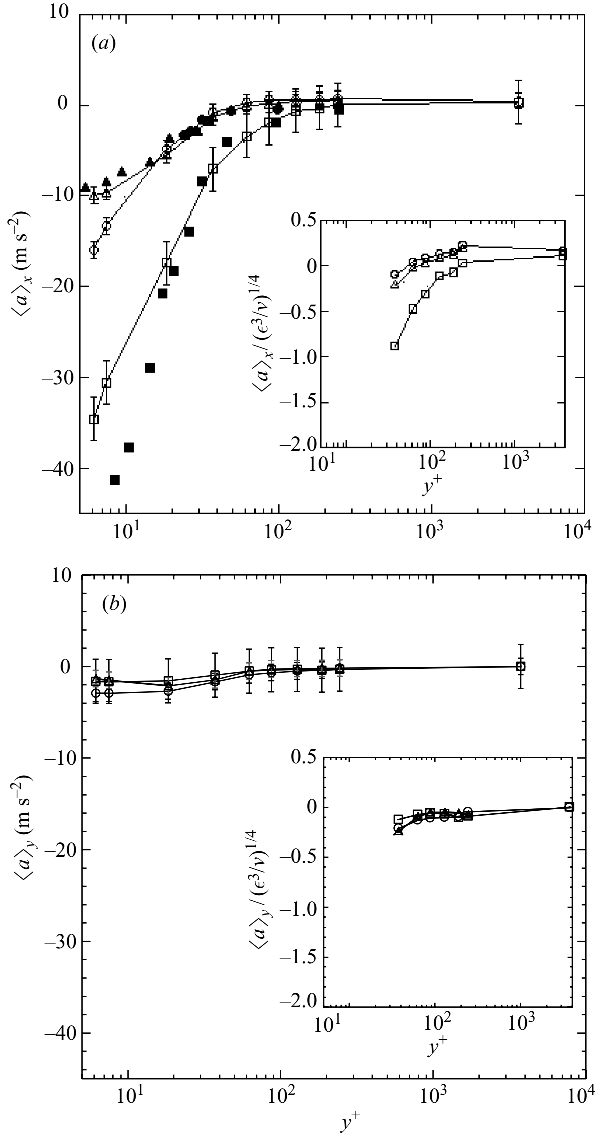

FIGURE 13. Mean accelerations *vs* y^+ of (*a*) the x and (*b*) y components: □, ■, $St_0 = 0.47$, $Re_{\lambda 0} = 240$; ○, $St_0 = 0.07$, $Re_{\lambda 0} = 240$; △, $St_0 = 0.035$, $Re_{\lambda 0} = 100$. Filled symbols in (*a*) are for the model (see § 5). Insets: mean accelerations normalized by $(\epsilon^3/\nu)^{1/4}$.

are playing a first-order role. Notice that the two low Stokes number cases have similar trends and magnitudes for the mean acceleration (figure 13), despite the different free-stream Reynolds numbers. We attribute the decrease in the magnitude of the mean acceleration (compared with the $St = 0.47$ case) to the decrease in inertial and gravitational effects. Intuition might have suggested that the magnitude of mean acceleration would decrease as inertia became more important. We will discuss this further in § 5 in terms of the effects of the mean shear. By comparison, the y mean component of acceleration is close to zero (figure 13*b*), with a small negative value close to the plate. The insets in figure 13 show the mean acceleration normalized by

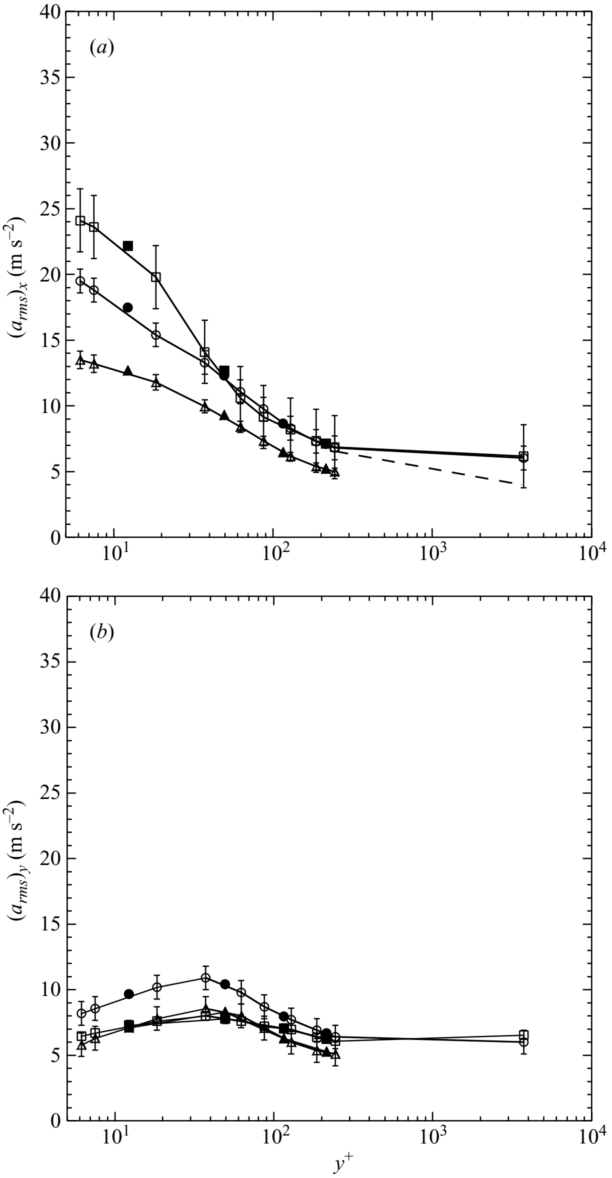

FIGURE 14. Acceleration r.m.s. *vs* y^+ for (*a*) x and (*b*) y components: squares, $St_0 = 0.47$, $Re_{\lambda 0} = 240$; circles, $St_0 = 0.07$, $Re_{\lambda 0} = 240$; triangles, $St_0 = 0.035$, $Re_{\lambda 0} = 100$. Filled symbols correspond to a strip width two times larger than for the open symbols.

$(\epsilon^3/\nu)^{1/4}$. Because of resolution difficulties in ϵ, the results extend only to $y^+ = 30$. The relative order of the three curves remains the same, except possibly for the y component where the differences are very small.

Figure 14 shows the r.m.s. acceleration as a function of y^+. As for the mean acceleration, the x-component, high Reynolds number ($Re_{\lambda 0} = 240$), high Stokes number case ($St_0 = 0.47$) has the highest magnitude close to the wall. For the two low Stokes number cases the acceleration r.m.s. is lower, but the $Re_{\lambda 0} = 240$ case has a higher r.m.s. acceleration than that of the lower ($Re_{\lambda 0} = 100$) case. Apparently the

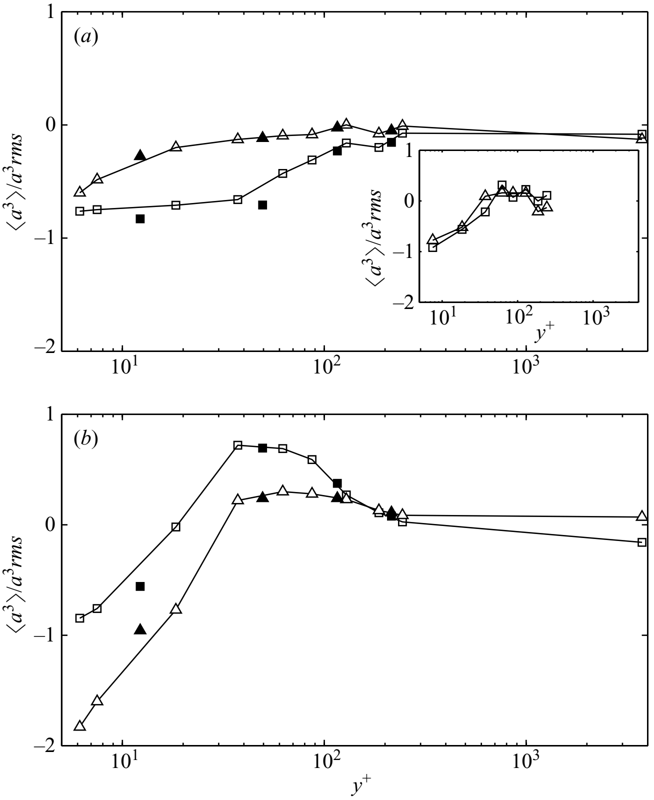

FIGURE 15. Skewness of the acceleration p.d.f.s. (*a*) $St_0 = 0.47, Re_{\lambda 0} = 240$ (inset: $St_0 = 0.28$, $Re_{\lambda 0} = 240$); (*b*) $St_0 = 0.07$, $Re_{\lambda 0} = 240$. For all plots: squares, x and triangles, y components. Filled symbols correspond to a strip width two times larger than for the open symbols.

higher level of turbulence near the wall is increasing the particle acceleration variance for the former case. The y component of the r.m.s. acceleration peaks at $y^+ \approx 30$ for all cases, and is significantly lower in magnitude than the x component. Notice that for this component the low stokes number, high Reynolds number case has the largest magnitude. As the free stream is approached the curve for the $Re_{\lambda 0} = 240$ must cross over that of the lower St case (for the same Reynolds number) since in isotropic turbulence the acceleration variance decreases with Stokes number (for the same Reynolds number). Thus the $St_0 = 0.47$, $Re_{\lambda 0} = 240$ case should have a lower r.m.s. value than that of $St_0 = 0.07$ at the same Reynolds number in the free stream. Our measurements show that at $y^+ \approx 4000$ the acceleration r.m.s. measured for $St_0 = 0.47$ and $St_0 = 0.07$ are approximately the same for $Re_{\lambda 0} = 240$ (figure 14*a*). The error in determining the acceleration r.m.s. in the free stream, where its value is small, is large for the high St case (see § 2) and the error bars do not rule out the possibility of the cross-over, as indicated by the dashed line within the error bar limits. Note that in these graphs (and the skewness graphs to be discussed), we have included estimates using different strip widths (§ 2) and the results are in good agreement, confirming that they are not sensitive to the width over which the acceleration is determined.

In figure 15 we plot the skewness of the acceleration p.d.f.s (figure 11) as a function of y^+ for the two high Reynolds number cases, $Re_{\lambda 0} = 240$, $St_0 = 0.47$ and

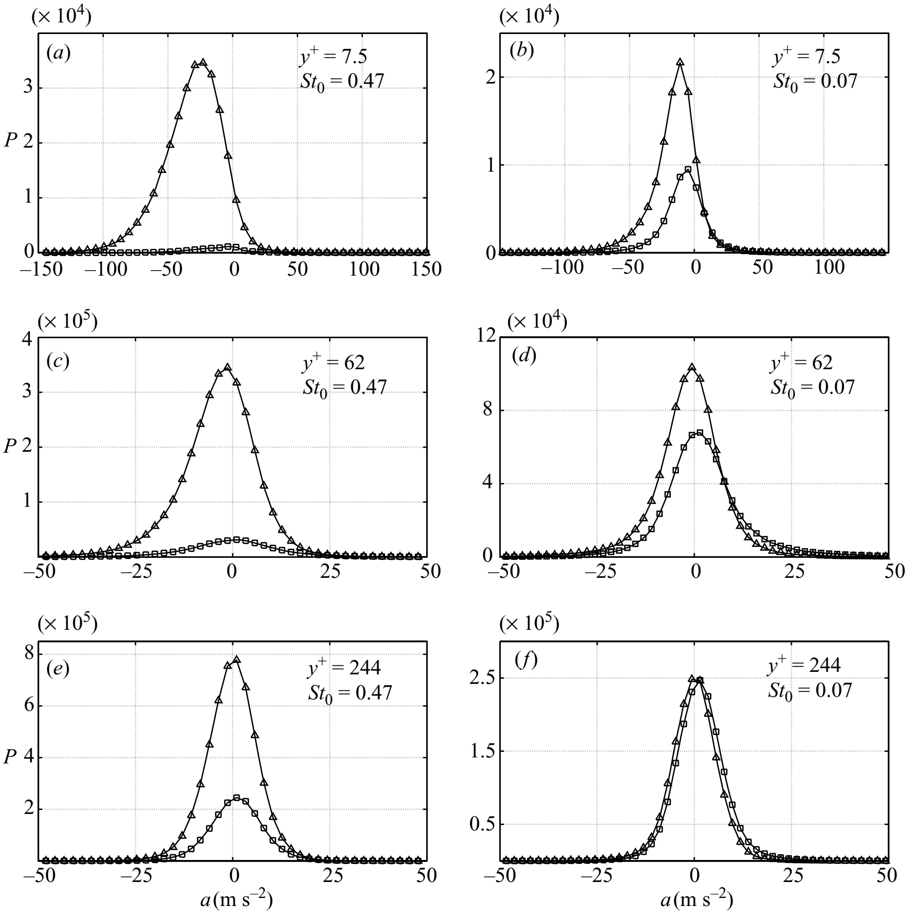

FIGURE 16. Conditional acceleration histograms of the x component at $Re_{\lambda 0} = 240$. △, v component of velocity is downward to plate; □, v component of velocity is upward from plate.

$St_0 = 0.07$. For the high St case the skewness is always negative, with that of the x component having a larger magnitude than that of the y component. For the low Stokes number case, the skewness becomes positive as y^+ increases (and then relaxes back to zero as the free stream is approached). For these cases, where inertial effects are less significant, the large positive acceleration events are more dominant than the decelerations at intermediate y^+. By changing the nozzle settings we took some extra measurements at an intermediate case, $Re_{\lambda 0} = 240$, $St_0 = 0.28$. Here the skewness behaviour was negative and rose to zero, qualitatively similar to the $St_0 = 0.07$ case but without an overshoot. This intermediate case, shown in the inset to figure 15(*a*), shows the continuous trend in skewness with Stokes number. Kurtosis values for the x component of acceleration showed large scatter. For $Re_{\lambda 0} = 240$, $St_0 = 0.47$ they were in the range 6 to 8 and for the $Re_{\lambda 0} = 240$ $St_0 = 0.07$ case they varied from 11 to 16 in the boundary layer.

The conditional histograms provide further insight into the behaviour of the acceleration. Figure 16 shows the histogram of the x component of acceleration conditioned on the sign of v, the vertical velocity, for two Stokes numbers and at three different distances from the plate. Close to the plate ($y^+ = 7.5$) the conditional histogram is dominated by the downward acceleration events, and this is more so for the high Stokes flow (compare figure 16*a* with figure 16*b*). Far from the plate ($y^+ = 244$) the downward events are still more dominant for the high Stokes number case (figure 16*e*), but for the low Stokes number case (figure 16*f*) upward and downward events are approximately equally probable.

5. Discussion

Our results show pronounced effects of the boundary layer structure on the Lagrangian acceleration statistics of inertial particles. We will discuss our observations in terms of the effects of the mean shear. First, we begin with a closer examination of the acceleration p.d.f.s.

As the wall is approached, the acceleration p.d.f.s become narrower and skewed (figure 11). This narrowing is most pronounced for the highest Stokes number. The Stokes number increases as y^+ decreases, and thus the decrease in the tails could be expected. The turbulence Reynolds number also decreases as the wall is approached and this will also affect the width of the tails. In this respect the particles in the boundary layer are behaving in a qualitatively similar way to their behaviour in isotropic turbulence, despite the boundary layer's more complex flow structure. However, in isotropic turbulence the acceleration variance decreases as the Stokes number increases due to the increase in the particle stopping time, τ_s (Ayyalasomayajula *et al.* 2006; Bec *et al.* 2006). In our boundary layer measurements, we find that both the mean acceleration and its variance become more pronounced with increasing Stokes number (figures 13 and 14), a result that is in marked contrast to the isotropic case. (In isotropic turbulence the mean acceleration must be zero, and this is observed in the outer part of our boundary layer, figure 13. Moreover, fluid particles ($St = 0$) should experience relatively weak mean acceleration in a zero-pressure-gradient flat-plate boundary layer.) Thus the observations of figures 13 and 14 must be explained in terms of the effects of boundary layer structure on the inertial particles. While there have been a number of studies of particle transfer mechanisms in the turbulent boundary layer (e.g. Kaftori *et al.* 1995*a*, *b*; Pan & Banerjee 1996; Young & Leeming 1997; Rouson & Eaton 2001; Marchioli & Soldati 2002) these papers focus on the effects of preferential particle concentration (in regions of the low-speed streaks) and on the effects of the sweeps and ejections on the particle transfer mechanisms. We have not been able to find any work that addresses directly the acceleration mechanisms for inertial particles.

While recognizing the importance of flow structure, we believe that by examining the effects of the mean shear and gravity we can shed light on the nature of the accelerations of the inertial particles. In the limiting case of a small rigid particle in a turbulent fluid, the equation of motion is (Maxey & Riley 1983)

$$\frac{\mathrm{d}\boldsymbol{X}}{\mathrm{d}t} = \boldsymbol{V}(t), \quad \frac{\mathrm{d}\boldsymbol{V}}{\mathrm{d}t} = -\frac{\boldsymbol{V}(t) - \boldsymbol{u}(\boldsymbol{X}(t), t)}{\tau_s} + \boldsymbol{g}. \tag{5.1}$$

Here $\boldsymbol{X}(t)$ is the particle position, $\boldsymbol{V}(t)$ is the particle velocity, $\boldsymbol{u}(\boldsymbol{X}(t), t)$ is the fluid velocity and $\boldsymbol{g}$ is acceleration due to gravity. We have neglected the Saffman lift force since we found it to be negligible compared to the other two terms for our flow. We have also neglected the ratio $(\rho_d - \rho_f)/\rho_d$ which is close to unity. For a fuller discussion of the relative importance of the terms in the equation of motion see

Elghobashi & Truesdell (1992). The solution for $\boldsymbol{V}(t)$ is (Bec *et al.* 2006)

$$\boldsymbol{V}(t) = \boldsymbol{V}(0)\mathrm{e}^{-t/\tau_s} + \int_0^t \mathrm{e}^{-(t-t')/\tau_s}\left(\frac{\boldsymbol{u}}{\tau_s} + \boldsymbol{g}\right)\mathrm{d}t'. \tag{5.2}$$

Taking the average of the y component of (5.2) and recognizing that $\langle u_y \rangle \approx 0$, we find for the mean vertical velocity of the inertial particles:

$$\langle V_y(t)\rangle = \langle V_y(0)\rangle \mathrm{e}^{-t/\tau_s} + g\tau_s(1 - \mathrm{e}^{-t/\tau_s}). \tag{5.3}$$

Integrating (5.3) with respect to time, we can write an expression for the average particle penetration distance, $\langle y_p \rangle$:

$$\langle y_p(t_p)\rangle = y_0 - \tau_s\langle V_y(0)\rangle\left(\mathrm{e}^{-t_p/\tau_s} - 1\right) + g\tau_s\left(t_p + \tau_s(\mathrm{e}^{-t_p/\tau_s} - 1)\right) \tag{5.4}$$

where t_p is the travel time between y_0 and y_p. We consider an arbitrary vertical position in the boundary layer, y_0, and from the tracks we take the mean vertical velocity at this position, $\langle V_y(0)\rangle$. Substituting these values and the value of τ_s at the same position (τ_s has slight dependence on y^+ since the particle size distribution depends on y^+ (see figure 9*a*)) into (5.4), and using the value of $\tau_{\eta 0}$ (the appropriate time scale for acceleration events) for t_p we can determine the particle penetration distance for each of the various conditions. Using these values and the shear the particle experiences over the penetration distance, we can write a relation for the mean particle acceleration:

$$\langle a \rangle_x \approx \frac{\langle V_x(y_p)\rangle - \langle V_x(y_0)\rangle}{\tau_{\eta 0}} \tag{5.5}$$

where $\langle V_x(y_p)\rangle$ and $\langle V_x(y_0)\rangle$ are the x velocity components of a particle taken from the mean velocity profile obtained from LDV measurements. This procedure has been carried out for a number of values of y^+. The results of our estimates are shown in figure 13 for the high and low Stokes number cases. The fit to the data is good. The above model suggests that the deceleration is due to the dissipative drag term which acts when the particles have a relative velocity compared with that of the fluid. The effect is enhanced when the shear is aligned with gravity. We note that this analysis holds for inertial particles only, and does not hold for $St \rightarrow 0$.

We now turn to the r.m.s. accelerations, figure 14. While we are unable to model their behaviour, it is instructive to check their magnitudes for consistency with other observations. In figure 17 we plot the x component of the acceleration variance normalized by $(\epsilon^3/\nu)^{1/2}$. Because of the large error bars, it is difficult to discern a clear trend although the low Reynolds number case falls below that of those at the high Reynolds numbers. We might expect that the high Stokes number case would have lower normalized acceleration value. This is the case in isotropic turbulence (Bec *et al.* 2006), but in the boundary layer the acceleration increases with St and this, although partially offset by the increased dissipation for the high Reynolds number case (figure 9*b*), apparently accounts for the slightly higher values of the normalized acceleration at the higher Stokes number. Note that the normalized accelerations only extend down to $y^+ = 30$ because of the uncertainty in the determination of the dissipation for smaller y^+. Thus there is little difference between the two different Stokes number cases for $Re_{\lambda 0} = 240$ since their acceleration variances only become significantly different below $y^+ = 30$ (figure 14). In isotropic turbulence the normalized acceleration variance, known as a_0 (Voth *et al.* 2002; Gylfason *et al.* 2004) is found to be in the range of 3 to 7 for fluid particles in the Reynolds number range of interest here. There is much scatter in the reported data, with the experiment showing higher

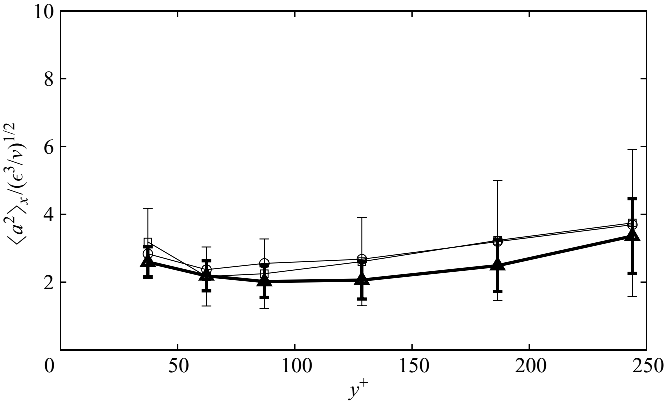

FIGURE 17. x component of the acceleration variance normalized by $(\epsilon^3/\nu)^{1/2}$. □, $St_0=0.47$, $Re_{\lambda 0}=240$; ○, $St_0=0.07$, $Re_{\lambda 0}=240$; △, $St_0=0.035$, $Re_{\lambda 0}=100$. The thick error bars are for $St_0=0.035$, $Re_{\lambda 0}=100$. The thin error bars are for $St_0=0.47$, $Re_{\lambda 0}=240$. To avoid clutter, no error bars are shown for $St_0=0.07$, $Re_{\lambda 0}=240$. They are the same as for $St_0=0.035$, $Re_{\lambda 0}=100$.

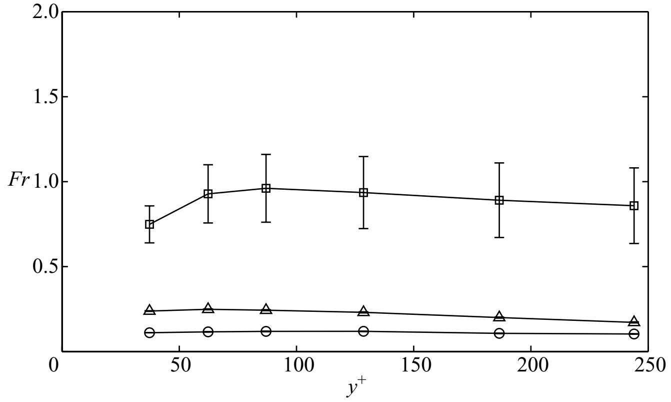

FIGURE 18. Froude number. □, $St_0=0.47$, $Re_{\lambda 0}=240$; ○, $St_0=0.07$, $Re_{\lambda 0}=240$; △, $St_0=0.035$, $Re_{\lambda 0}=100$.

values than DNS (Gylfason *et al.* 2004). Thus our measurements, with values around 4 and decreasing with decreasing y^+, are in the same range as the isotropic results but further work will be needed to separate Reynolds, Stokes and gravitational effects as well as the effects of anisotropy caused by the shear. In figure 18 we plot the Froude number $Fr=gSt/a_{rms}$. Since this depends on the estimation of acceleration, the error bars are large for the high Stokes number case. The trend and magnitude follow that of u_g/u_η (figure 10). Note that the ratio $Fr/(u_g/u_\eta)$ is ${a_0}^{-1/2}$.

Finally, we remark on the forms of the acceleration r.m.s. profiles. As mentioned we do not have other experimental or DNS results with which to compare our inertial particle acceleration results. However, the DNS acceleration profiles for turbulent channel flow by Choi, Yeo & Lee (2004*a*, *b*) show similar form to our r.m.s. profiles of figure 14. Thus they show that the x component increases until very close to the wall, and the y component has its maximum at y^+ of approximately 30 and is smaller in magnitude than the x component. This is consistent with our own observations (figure 14), although, as we have emphasized, inertia plays a dominant role in our flow and the physics as $St \to 0$ may be different. However the boundary structure must affect the acceleration fluctuations. Thus we would expect the sweeps and ejection mechanisms and the other concomitant motions to be reflected in the inertial particle flutuations.

6. Conclusions

Using high-speed particle tracking techniques, we have shown the pronounced effects of shear on the Lagrangian acceleration statistics of inertial particles in a turbulent boundary layer. Results from three different cases have been presented in order to form a consistent set: low and high Stokes numbers with the same free-stream Reynolds number, and approximately the same Stokes number at different free-stream Reynolds numbers. Our findings suggest that the acceleration statistics are primarily determined by the particle inertia and the boundary layer structure, specifically shear. We determined that changes of the free-stream turbulence conditions and particle injection methods were not critical for the qualitative behaviour of the acceleration statistics.

Our main finding is that the magnitude of the acceleration mean and its r.m.s. increase as the boundary layer wall is approached (figures 13 and 14). Here shear and Stokes number effects become large and these act to strongly decelerate the particles. The acceleration p.d.f.s become narrower and skewed, reflecting the increasing Stokes numbers and shear as the wall is approached (figure 11). We note that in isotropic turbulence, as the Stokes numbers increases, the r.m.s. acceleration decreases (Bec *et al.* 2006; Ayyalasomayajula *et al.* 2006), in marked contrast to the present findings. We have further quantified the p.d.f. statistics by determining the acceleration p.d.f. conditioned on the vertical velocity, showing that vertically downward accelerations dominate upward ones, and that this is more pronounced for higher Stokes number (figure 16). We have compared our results from the outer part of the boundary layer (where shear effects are weak) to our earlier measurements (Ayyalasomayajula *et al.* 2006) using a different optical setup, and the measurements agree well (figure 11*b*). We have also provided estimates of the normalized acceleration variance (figure 17) and have compared them with values observed in isotropic turbulence. We have used the equations of motion for a Lagrangian particle to model the mean acceleration. From these we have shown the importance of the effects of shear coupled with inertia and gravity.

We believe our results will be of significance to the modelling of natural as well as industrial processes where shear is often present and particles are integral to the process. These include dust and salt particles in the atmospheric boundary layer, droplets in clouds, phytoplankton behaviour in the oceans and reactions and transport in gas turbine combustors, but there are many other examples. The subject is complex since there are a number of parameters. Shear strength, particle distribution, Stokes number, Reynolds number and Froude number all undoubtedly play a role in determining the behaviour of the small inertial particles described here and systematic experimental and computational work will be required in order to determine their relative effects. We should expect further complications for particles larger than the Komogorov scale since there is already evidence that the acceleration p.d.f.s for this case behave differently to those of small particles in flows without shear (Xu & Bodenschatz 2008; Qureshi *et al.* 2007). The subject is rich and there is much to be done.

Our results appear to be the first Lagrangian acceleration measurements of inertial particles in a turbulent shear flow. The flow we have addressed here is complex and it will be of importance to see if the observations reported here are qualitatively reproduced in channel flow or in homogeneous shear flow.

We thank Armann Gylfason and Sathyanarayana Ayyalasomayajula for their advice on the experiment and Lance Collins, Eberhard Bodenschatz, Juan Salazar, Greg Voth, Haitao Xu, Greg Bewley and the reviewers for their comments and suggestions. The work was carried out in the DeFrees wind tunnel at Cornell University. We thank Todd Cowen for the use of the tunnel. This work was supported by the US National Science Foundation.

REFERENCES

Aliseda, A., Cartellier, A., Hainaux, F. & Lasheras J. C. 2002 Effect of preferential concentration on the settling velocity of heavy particles in homogeneous isotropic turbulence. *J. Fluid Mech.* **468**, 77–105.

Ayyalasomayajula, S. Collins, L. R. & Warhaft, Z. 2008 Modelling inertial particle Lagrangian acceleration statistics in turbulent flows. *Phys. Fluids* **20**, 095104.

Ayyalasomayajula, S., Gylfason, A., Collins, L. R., Bodenschatz, E. & Warhaft, Z. 2006 Lagrangian measurements of inertial particle accelerations in grid generated wind tunnel turbulence. *Phys. Rev. Lett.* **97**, 144507.

Bec, J., Biferale, L. Boffetta, G., Celani, A., Cencini, M., Lanotte, A., Musacchio, S. & Toschi, F. 2006 Acceleration statistics of heavy particles in turbulence. *J. Fluid Mech.* **550**, 349–358.

Bourgoin, M., Ouellette, N. T., Xu, H. T., Berg, J. & Bodenschatz, E. 2006 The role of pair dispersion in turbulent flow. *Science.* **311**, 835–838.

Brooke, J. W., Kontomaris, K., Hanratty, T. J. & McLaughlin, J. B. 1992 Turbulent deposition and trapping of aerosols at a wall. *Phys. Fluids* A. **4**, 825–834.

Chen L., Goto S. & Vassilicos, J. C. 2006 Turbulent clustering of stagnation points and inertial particles. *J. Fluid Mech.* **553**, 143–154.

Choi, J., Yeo, K. & Lee, C. 2004*a* Intermittent nature of acceleration in near wall turbulence. *Phys. Rev. Lett.* **92**, 144502.

Choi, J., Yeo, K. & Lee, C. 2004*b* Lagrangian statistics in turbulent channel flow. *Phys. Fluids* **16**, 779–793.

Christensen, K. T. & Adrian, R. J. 2002 Measurement of instantaneous Eulerian acceleration fields by particle-image velocimetry: method and accuracy. *Exps. Fluids* **33**, 759–769.

Chun, J. H., Koch D. L., Rani S. L., Ahluwalia A. & Collins L. R. 2005 Clustering of aerosol particles in isotropic turbulence. *J. Fluid Mech.* **536**, 219–251.

DeGraaff, D. B. & Eaton, J. K. 2000 Reynolds-number scaling of the flat-plate turbulent boundary layer. *J. Fluid Mech.* **422**, 319–346.

Dong, P., Hsu, T. Y., Atsavapranee, P. & Wei, T. 2001 Digital particle image accelerometry. *Exps. Fluids* **30**, 626–632.

Elghobashi, S. & Truesdell, G. C. 1992 Direct simulation of particle dispersion in a decaying isotropic turbulence. *J. Fluid Mech.* **242**, 655–700.

Elperin, T., Kleeorin, N., L'vov, V. S., Rogachevskii, I. & Sokoloff, D. 2002 Clustering instability of the spatial distribution of inertial particles in turbulent flows. *Phys. Rev.* E **66**, 036302.

Friedlander, S. K. & Johnstone, H. F. 1957 Deposition of suspended particles from turbulent gas streams. *Indust. Engng Chem.* **49**, 1151–1156.

Fuchs, W., Nobach, H. & Tropea C. 1994 Laser Doppler anemometry data simulation: application to investigate the accuracy of statistical estimators. *AIAA J.* **32**, 1883–1889.

Ghosh, S., Davila, J., Hunt, J. C. R., Srdic, A., Fernando, H. J. S. & Jonas, P. R. 2005 How turbulence enhances coalescence of settling particles with applications to rain in clouds. *Proc. R. Soc. Lond.* A. **461**, 3059–3088.

Goto, S. & Vassilicos, J. C. 2008 Sweep-stick mechanism of heavy particle clustering in fluid turbulence. *Phys. Rev. Lett.* **100**, 054503.

Gulitski, G., Kholmyansky, M., Kinzelbach, W., Luthi, B., Tsinober, A. & Yorish, S. 2007 Velocity and temperature derivatives in high Reynolds number turbulent flows in the atmospheric surface layer. Part 2. Acceleration and related matters. *J. Fluid Mech.* **589**, 83–102.

Gylfason, A. 2006 Particles, passive scalars, and the small scale structure of turbulence. PhD Thesis. Mechanical and Aerospace Engineering, Cornell University.

Gylfason, A., Ayyalasomayajula, S. & Warhaft, Z. 2004 Intermittency, pressure and acceleration statistics from hot-wire measurements in wind-tunnel turbulence. *J. Fluid Mech.* **501**, 213–229.

Hancock, P. E. & Bradshaw, P. 1989 Turbulence structure of a boundary layer beneath a turbulent free stream. *J. Fluid Mech.* **205**, 45–76.

Hill, R. J. & Wilczak, J. M. 1995 Pressure structure functions and spectra for locally isotropic turbulence. *J. Fluid Mech.* **296**, 247–269.

Jakobsen, M. L., Dewhirst, T. P. & Greated, C. A. 1997 Particle image velocimetry for predictions of acceleration fields and force within fluid flows. *Meas. Sci. Technol.* **8**, 1502–1516.

Jensen, A., Sveen, J. K., Grue, J., Richon, J. B. & Gray, C. 2001 Accelerations in water waves by extended particle image velocimetry. *Exps. Fluids* **30**, 500–510.

Kaftori, D., Hetsroni, G. & Banerjee, S. 1995*a* Particle behavior in the turbulent boundary layer. Part I: Motion, deposition, and entrainment. *Phys. Fluids* **7**, 1095–1106.

Kaftori, D., Hetsroni, G. & Banerjee, S. 1995*b* Particle behavior in the turbulent boundary layer. Part II: Velocity and distribution profiles. *Phys. Fluids* **7**, 1007–1121.

Kinzel, M., Nobach, H., Tropea, C. & Bodenschatz, E. 2006 Measurement of Lagrangian acceleration using the laser Doppler technique. *Proc. 13th Intl Symp. on Applications of Laser Techniques to Fluid Mechanics, June 26–29, Lisbon, Portugal.*

Kulick, J. D, Fessler, J. R. & Eaton, J. K. 1994 Particle response and turbulence modification in fully developed channel flow. *J. Fluid Mech.* **277**, 109–134.

Lehmann, B., Nobach, H. & Tropea, C. 2002 Measurement of acceleration using the laser Doppler technique. *Meas. Sci. Technol.* **13**, 1367–1381.

Lehmann, K., Siebert, H., Wendisch, M. & Shaw, R. 2007 Evidence for inertial droplet clustering in weakly turbulent clouds. *Tellus* B **59**, (1), 57–65.

Liu, X. & Katz, J. 2006 Instantaneous pressure and material acceleration measurements using a four-exposure PIV system. *Exps. Fluids* **41**, 227–240.

Lowe, T. K. & Simpson, R. L. 2006 Measurements of velocity-acceleration statistics in turbulent boundary layers. *Intl J. Heat Fluid Flow* **27**, 558–565.

Makita, H. 1991 Realization of a large-scale turbulence field in a small wind-tunnel. *Fluid Dyn. Res.* **8**, 53–64.

Marchioli, C. & Soldati, A. 2002 Mechanisms for particle transfer and segregation in a turbulent boundary layer. *J. Fluid. Mech.* **468**, 283–315.

Maxey, M. R. 1987 The gravitational settling of aerosol particles in homogeneous turbulence and random flow fields. *J. Fluid Mech.* **174**, 441–465.

Maxey, M. R. & Riley, J. J. 1983 Equation of motion for a small rigid sphere in a non-uniform flow. *Phys. Fluids* **26**, 883–889.

Mordant, N., Crawford, A. & Bodenschatz, E. 2004 Experimental lagrangian acceleration probability density function measurements. *Physica* D **193**, 245–251.

Mordant, N., Metz, P., Michel, O. & Pinton, J. F. 2001. Measurement of Lagrangian velocity in fully developed turbulence. *Phys. Rev. Lett.* **87**, 214501.

Mydlarski, L. & Warhaft Z. 1996 On the onset of high-Reynolds-number grid-generated wind tunnel turbulence. *J. Fluid Mech.* **320**, 331–368.

Ouellette, N. T., Xu, H. & Bodenschatz, E. 2006*a* A quantitative study of three-dimensional Lagrangian particle tracking algorithms. *Exps Fluids* **40**, 301–313.

Ouellette, N. T., Xu, H., Bourgoin, M. & Bodenschatz, E. 2006*b* Small-scale anisotropy in Lagrangian turbulence. *New J. Phys.* **8**, 102–111.

Pan, Y. & Banerjee, S. 1996 Numerical simulation of particle interactions with wall turbulence. *Phys. Fluids* **8**, 2733–2755.

Post, S. L. & Abraham, J. 2002 Modeling the outcome of drop-drop collisions in Diesel sprays. *Intl J. Multiphase Flow* **28**, 997–1019.

Qureshi, N. M., Bourgoin, M., Baudet, C., Cartellier, A. & Gagne, Y. 2007 Turbulent transport of material particles: An experimental study of finite size effects. *Phys. Rev. Lett.* **99**, 184502.

Rouson, D. W. I. & Eaton, J. K. 2001 On the preferential concentration of solid particles in turbulent channel flow. *J. Fluid Mech.* **428**, 149–169.

Salazar, J. P. L. C., de Jong J., Cao, L., Woodward, S., Meng, H. & Collins, L. R. 2008 Experimental and numerical investigation of inertial particle clustering in isotropic turbulence. *J. Fluid Mech.* **600**, 245–256.

Saw, E. W., Shaw, R., Ayyalasomayajula, S., Chuang, P. Y. & Gylfason, A. 2008 Inertial Clustering of Particles in High-Reynolds-Number Turbulence. *Phys. Rev. Lett.* **100**, 214501.

Seuront, L. & Schmitt, F. G. 2004 Eulerian and Lagrangian properties of biophysical intermittency in the ocean. *Geophys. Res. Lett.* **31**, L03306.

Shaw, R. A. 2003 Particle-turbulence interactions in atmospheric clouds. *Annu. Rev. Fluid Mech.* **35**, 183–227.

Shen, X. & Warhaft, Z. 2000 The anisotropy of the small scale structure in high Reynolds number (R-lambda similar to 1000) turbulent shear flow. *Phys. Fluids.* **12**, 2976–2989.

Squires, K. D. & Eaton, J. K. 1991 Preferential concentration of particles by turbulence. *Phys. Fluids* A **3**, 1169–1178.

Sundaram, S. & Collins, L. R. 1997 Collision statistics in an isotropic particle-laden turbulent suspension. Part 1. Direct numerical simulations. *J. Fluid Mech.* **335**, 75–109.

Thole, K. A. & Bogard, D. G. 1996 High free stream turbulence effects on turbulent boundary layers. *J. Fluids Engng* **118**, 276–284.

Toschi, F. & E Bodenschatz, E. 2009 Lagrangian properties of turbulence. *Annu. Rev. Fluid Mech.* (in press).

Tsuji, Y., Fransson, J. H. M., Alfredsson, P. H. & Johansson, A. V. 2007 Pressure statistics and their scaling in high-Reynolds-number turbulent boundary layer. *J. Fluid Mech.* **585**, 1–40.

Volk, R., Mordant, N., Verhille, G. & Pinton, J. F. 2008 Laser Doppler measurement of inertial particle and bubble accelerations in turbulence. *Europhys. Lett.* **81**, 34002.

Voth, G. A., La Porta, A., Crawford, A. M., Alexander, J. & Bodenschatz, E. 2002 Measurement of particle accelerations in fully developed turbulence. *J. Fluid Mech.* **469**, 121–160.

Wood, A. M., Hwang, W. & Eaton, J. K. 2005 Preferential concentration of particles in homogeneous and isotropic turbulence. *Intl J. Multiphase Flow* **31**, 1220–1230.

Xu, H. & Bodenschatz E. 2008 Motion of inertial particles with size larger than the Komogorov scale in turbulent flows. *Physica D.* doi:10.1016/j.physd.2008.04.022

Xu, H., Bourgoin, M., Ouellette, N. T. & Bodenschatz E. 2006 High order Lagrangian velocity statistics in turbulence. *Phys. Rev. Lett.* **96**, 024503.

Xu, H., Ouellette, N. T. & Bodenschatz E. 2008 Evolution of geometric structures in intense turbulence. *New J. Phys.* **10**, 013012.

Young, J. & Leeming, A. 1997 A theory of particle deposition in a turbulent pipe flow. *J. Fluid Mech.* **340**, 129–159.